Structural Complexity and High Thermoelectric Performance of the Zintl Phase: $Yb_{21}Mn_4Sb_{18}$

Allan He[a], Sabah K. Bux[b], Yufei Hu[a], David Uhl[b], Li Li[a,c], Davide Donadio[a], Susan M. Kauzlarich*[a]

[a]Department of Chemistry, University of California, One Shields Avenue, Davis, California 95616

[b]Jet Propulsion Laboratory, California Institute of Technology, 4800 Oak Grove Drive, MS 277-207, Pasadena, CA 91125, USA

[c]State Key Laboratory of Coordination Chemistry, School of Chemistry and Chemical Engineering, Collaborative Innovation Center of Advanced Microstructures, Nanjing University, Nanjing 210023, P. R. China

Abstract

Thermoelectric materials are a unique class of compounds that can recycle energy through conversion of heat into electrical energy. A new 21-4-18 Zintl phase has been discovered in the Yb-Mn-Sb system with high performance in the mid-to-high temperature regime. The efficiency of $Yb_{21}Mn_4Sb_{18}$ results mainly from its large Seebeck coefficient (~290 μV/K at 650K) and extremely low thermal conductivity (~0.4 $Wm^{-1}K^{-1}$). The complex crystal structure has been studied through single crystal X-ray diffraction, synchrotron powder X-ray diffraction, and pair distribution function (PDF) analysis using time-of-flight neutron diffraction revealing positional disorder on several sites. Electronic structure calculations of the band structure and the partial spin-density of states reveal that states near the Fermi level are contributed mostly by the Mn and Sb atoms that participate in the $[Mn_4Sb_{10}]^{22-}$ motif of the structure. The band structure confirms the p-type semiconducting nature of this material. Optimization of hole carrier concentration was tuned according to a single parabolic band model through Na doping on the Yb site ($Yb_{21-x}Na_xMn_4Sb_{18}$, x = 0, 0.2, 0.4) showing an improvement in zT over the whole temperature range. A maximum zT ≈ 0.8 at 800K is obtained for the x = 0.4 sample and increases ZT_{avg} from 0.34 to 0.49 (over the entire temperature range) compared to the undoped sample.

Introduction

Thermoelectric materials are a class of materials that can harvest energy by converting heat into electricity. Their unique ability has found many applications in industry including: the use of Peltier coolers to replace gas-based refrigeration technology thereby eliminating the use of chlorofluorocarbons, waste heat recovery in automobiles to increase fuel efficiency, as well as in deep-space missions where long-term, reliable power generation is necessary for on-board instruments. In order to deploy its full potential and to make thermoelectric technology more widespread, materials with higher thermoelectric efficiency must be discovered. The performance of a material is based on its figure of merit, zT (**Equation 1**):

$$zT = \frac{\alpha^2 T}{\rho(\kappa_l + \kappa_e)} \tag{1}$$

where α, T, ρ, κ_l, κ_e are the Seebeck coefficient, temperature, resistivity, lattice and electrical components of the thermal conductivity, respectively.

Zintl phases have shown to be a very fruitful category for thermoelectric material discovery.[1,2] Typically, they are defined as semiconducting, charge balanced compounds with complete electron transfer between the more electropositive donor and the electronegative acceptor.[3,4] The electrons provided by the electropositive elements are sometimes not enough to compensate the more electronegative counterpart, thus leading to the formation of covalent bonding frameworks between anions. This combination of ionic and covalent bonding can lead to complex structure types (e.g. $Yb_{14}MnSb_{11}$,[5-8] $Zn_{13}Sb_{10}$,[9-11] $Ba_8Ga_{16}Ge_{30}$,[12,13] $CeFe_4Sb_{12}$[14] to name a few) with intrinsically low thermal conductivity, making these materials a great starting point for optimization.

Currently in literature, Zintl phase structures with composition $A_{21}M_4Pb_{18}$ (referred to as 21-4-18) have been reported such as: $A_{21}Cd_4Pn_{18}$ (A = Eu, Sr, Ba; Pn = Sb, Bi),[15] $A_{21}Zn_4Pn_{18}$ (A = Ca, Eu; Pn = As, Sb),[16] and $Ca_{21}Mn_4(Sb,Bi)_{18}$.[17,18] There are several different structure types within this class of compounds, which crystallize in space groups *C*2/*c*, *C*2/*m* and *Cmce*. The structures all contain MPn_4 tetrahedral units linked in various manners. Attention has been paid mainly to the structural and magnetic properties of these complex phases; however, their thermoelectric properties have yet to be characterized. Here, we report the structural and thermoelectric properties for a new member of the 21-4-18 family: $Yb_{21}Mn_4Sb_{18}$, with high figure of merit in the mid-to-high temperature regime. $Yb_{21}Mn_4Sb_{18}$ adds a new composition to this class of Zintl phases, crystallizing in the α-$Ca_{21}Mn_4Sb_{18}$ structure type (monoclinic, space group *C2/c*). The *C*2/*c* structure can be described as containing 4 discrete units per formula unit: 1 linear $[Mn_4Sb_{10}]^{22-}$ anion, 2 dumbbell-shaped $[Sb_2]^{4-}$ anions, 4 individual Sb^{3-} anions, and 21 Yb^{2+} cations (see **Figure S1**, in Supporting Information (**SI**)). The expected low thermal conductivity, due to the large primitive cell, and potentially high Seebeck, because of the high density of states close to the Fermi level,[18] make this phase a good starting point for optimization of thermal and electrical transport properties. Optimization of $Yb_{21}Mn_4Sb_{18}$ was pursued through shifting of the Fermi level by changing the carrier concentration. The single parabolic band model was used to approximate the optimum carrier concentration and was accomplished through Na doping on the Yb site ($Yb_{21-x}Na_xMn_4Sb_{18}$, x = 0, 0.2, 0.4).

Experimental

Synthesis of $Yb_{21}Mn_4Sb_{18}$

Bulk powder samples were synthesized through mechanical milling for homogenization and spark plasma sintering for densification. Stoichiometric amounts of Yb filings (Metall Rare Earth Limited, 99.99%), Mn pieces (Alfa Aesar, 99.95%), Sb shots (Alfa Aesar, 99.999%) were placed inside a stainless steel ball-mill with total sample mass of 10 g. The ball-mill was heat sealed inside a Mylar bag and the materials were homogenized for one hour in a SPEX 8000 M High-Energy Ball Mill. The resultant mixture was ground thoroughly with an agate mortar and pestle inside an Ar atmosphere drybox (<1 ppm H_2O) and milled for an additional hour, as described above. The powder was transferred into 8 cm long Nb tubes inside the glovebox and sealed in an arc-welder under partial Ar pressure. The Nb tubes were further encapsulated inside evacuated fused silica tubes. The reaction vessel was heated at 100°C/h to 650°C, sintered for 7 days, and allowed to slowly cool down to room temperature in the furnace.

The reaction vessel was then transferred and opened in a drybox, ground finely, and the sintered powder was filtered through a 200 mesh sieve. Approximately 3g of material was put into a 12.7 mm graphite die with graphite spacers and transferred into the chamber of a Dr. Sinter SPS-2050 spark plasma sintering (SPS) system for densification. Prior to starting the heating profile, the chamber was evacuated until ~10 Pa, and a pressure of 6 kN was applied onto the die. To prevent overshooting, the temperature was first increased to 525°C in 15 minutes, followed by an increase to 575°C in 1 minute where it stayed for 30 minutes. The displacement of the die was monitored closely and upon compression of the material (~430°C), the pressure was adjusted monotonically to 11 kN.

Single crystal growth was successful using Pb flux. Elemental Yb metal filings (Metall Rare Earth Limited, 99.99%), Mn pieces (Alfa Aesar, 99.95%), Sb shots (Alfa Aesar, 99.999%), and Pb shots (Alfa Aesar, 99.99%) were loaded into Al_2O_3 crucibles[19] in 21:4:18:80 ratio. Generous amounts of quartz wool were placed on both the top and bottom of the crucible and the reaction was sealed into evacuated quartz ampoules. The sample was heated to 500°C at 120°C/h (2h dwell), and afterwards brought to 700°C at 120°C/h before cooling down to 400°C at 2°C/h. The sample was quickly heated to 500°C and the molten flux was removed through centrifugation. Small single crystals were obtained which appeared irregularly shaped, black and reflective (see **Figure S2**).

Single Crystal X-ray Diffraction

Single crystal diffraction data were obtained on $Yb_{21}Mn_4Sb_{18}$ at 100K using a Bruker APEX II diffractometer with Mo Kα ($\lambda = 0.71073$ Å) radiation. Crystals were chosen under mineral oil and mounted on MiTeGen microloops. Space group determination was done using XPREP, and structural solutions were completed through direct methods with SHELXS and refined using the SHELXL software.[20]

Synchrotron X-ray Powder Diffraction

Synchrotron data were collected at the 11-BM-B beamline of the Advanced Photon Source (APS) at Argonne National Laboratory (ANL) with $\lambda = 0.412736$ Å at room temperature. The sample was placed into Kapton capillaries and the scattering data were collected in transmission mode. The large absorption coefficient of this material (51.279 mm^{-1}) required dilution of the sample with SiO_2 (approx. 1:80 ratio of $Yb_{21}Mn_4Sb_{18}$:SiO_2) to mitigate problems during Rietveld analysis.

Compositional analysis

Samples were mounted in discs of epoxy resin and polished to a 0.05 μm finish. Elemental analysis was characterized through energy dispersive spectroscopy (EDS) using a FEI Scios DualBeam SEM/FIB with a window-less Oxford Instruments X-max50, 50 mm^2 silicon drift detector. Secondary electron images were collected with an accelerating voltage of 20 kV using an Everhart-Thornley Detector. Elemental mapping was performed on the pelletized samples to check homogeneity. Samples were cross-checked with electron microprobe analysis (EMPA) to verify the composition of the $Yb_{21}Mn_4Sb_{18}$ phase. Quantitative elemental analysis was performed using a Cameca SX-100 Electron Probe Microanalyzer with wavelength-dispersive spectrometers using 15 kV accelerating potential. Compositions of samples were characterized with respect to calibrated standards of $Yb_{14}MnSb_{11}$, Sb metal, and Mn metal.

Time-of-flight Neutron Powder Diffraction

Time-of-flight neutron scattering data were collected on the NOMAD powder diffraction beamline at the Spallation Neutron Source (SNS) of Oak Ridge National Laboratory (ORNL) at room temperature. The polycrystalline sample was placed inside 3 mm diameter quartz capillaries for the total scattering experiment. NOMAD data were reduced using beamline software[21] to be used for Rietveld refinement and pair distribution function (PDF) analysis. The reduced pair distribution function (G(r), **Equation 2**) was obtained through a sine Fourier transformation of S(Q) according to:

$$G(r) = 4\pi r[\rho(r) - \rho_0] = \frac{2}{\pi}\int_0^\infty Q[S(Q) - 1]\sin(Qr)\,dQ \qquad (2)$$

where $\rho(r)$ represents the atomic pair density and ρ_0 is the average atomic number density. Neutron diffraction data and PDF refinement were performed with TOPAS software v5 and PDFgui.[22]

Thermoelectric property measurements

A Linseis LSR-3 instrument was used to measure resistivity and Seebeck coefficient employing the four-probe method from 350K to 800K under He atmosphere. The sample measured was bar-shaped (~10 mm x 2 mm x 2 mm) using 8 mm probes, and polished prior to measurement. Multiple samples were measured to ensure reproducibility and the data was cross-checked by measurements at JPL. There, the Seebeck coefficient was measured using a light pulse technique as described in the following reference using W/Nb thermocouples.[23] Electrical resistivity (ρ) was measured using the van der Pauw (VDP) technique with a current of 100 mA and the Hall coefficient was measured with a 0.75 T field and tungsten pressure contacts under high vacuum.[24]

A Netzsch LFA 457 was used to measure thermal diffusivity under vacuum up to 800 K on sample disks, polished flat and coated with graphite. Heat capacity was estimated using the Dulong-Petit method to calculate thermal conductivity.

Electronic Structure Theory

Spin-polarized total energy and electronic band structure calculations were carried out using density functional theory (DFT) with a semilocal exchange and correlation functional in the generalized gradient approximation.[25] The Kohn-Sham orbitals for the valence electrons are expanded on a plane wave basis set with a cutoff energy of 45 Ry, and the core electrons, including the *f*-electrons of Yb, are taken into account by Project Augmented Wave pseudopotentials. The first Brillouin zone of the 86-atom primitive cell is integrated over a uniform 4x4x3 k-points mesh[26] in the geometry optimization run and over a thicker 6x6x4 k-point mesh for the subsequent self-consistent electronic structure calculations. All the calculations are carried out using the open-source Quantum-Espresso package v6.3.[27]

Results and Discussion

Yb-Mn-Sb Systems

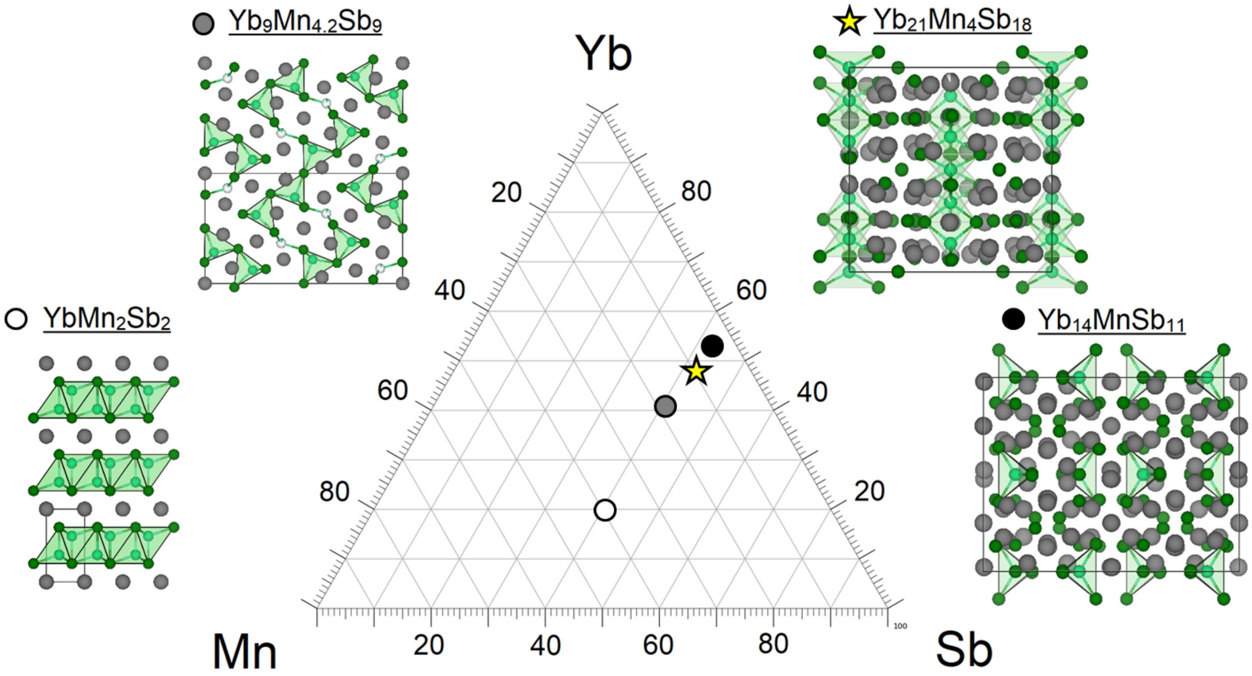

Figure 1: Phase diagram of current existing compounds in the Yb-Mn-Sb ternary system. The $YbMn_2Sb_2$, $Yb_9Mn_{4.2}Sb_9$, $Yb_{21}Mn_4Sb_{18}$, $Yb_{14}MnSb_{11}$ phases are indicated with open circle, grey circle, star, black circle respectively.

An extensive amount of work has already been reported for the Yb-Mn-Sb system on the $YbMn_2Sb_2$ phase,[28] the $Yb_9Mn_{4+x}Sb_9$ phase,[29-31] and the $Yb_{14}MnSb_{11}$ phase.[5-8] The composition for $Yb_{21}Mn_4Sb_{18}$ is indicated by a star in **Figure 1**. An overarching structural theme among these phases is the $MnSb_4$ tetrahedra that are either isolated or linked in various manners. The progression of the structure and bonding of these tetrahedra with the stoichiometry change is shown in **Figure 1**. The $YbMn_2Sb_2$ structure consists of covalently bonded Mn – Sb tetrahedra layers with Yb^{2+} occupying the interplanar spacings. As we move to the more Mn deficient $Yb_9Mn_{4+x}Sb_9$ phase, the crystal structure changes to form interconnected ribbons of the Mn – Sb tetrahedra. More Mn deficient still, is the 21-4-18 phase, where the infinitely connected chains of Mn-Sb tetrahedra start to become disconnected entities. The signature 21-4-18 structural motif are the $[Mn_4Sb_{10}]^{22-}$, edge-sharing tetramer units that extend along the b-axis, indicated by the green polyhedra. Finally, in the most Mn deficient phase so far in the Yb-Mn-Sb system, the $Yb_{14}MnSb_{11}$ phase, the large number of Sb atoms to Mn brings about the appearance of $[Sb_3]^{7-}$ trimers and isolated $[MnSb_4]^{9-}$ tetrahedra. It has been demonstrated that $Yb_{14}MnSb_{11}$ is one of the best p-type thermoelectric materials in the high temperature region (800-1200 K) because of its low electrical resistivity and thermal conductivity.[7]

Crystal Structure

Structural solution and refinement of single crystal data (results summarized in **SI**, **Table S1**) show that $Yb_{21}Mn_4Sb_{18}$ (**Figure 2**) crystallizes with monoclinic symmetry (space group *C2/c*). In the ordered structure, there are a total of 24 crystallographic sites (11 Yb sites, 9 Sb sites, and 4 Mn sites). Included in the unit cell are: a $[Mn_4Sb_{10}]^{22-}$ unit (two tetramer units shown linked through the octahedral Yb11 atom), 2 $[Sb_2]^{4-}$ dimers, 4 isolated Sb^{3-} anions, and 21 Yb^{2+}, satisfying the Zintl-Klemm formalism of being a charge balanced compound. The $[Mn_4Sb_{10}]^{22-}$ subunits are composed of edge-shared $MnSb_4$ tetrahedra and are an overarching motif of the α-$Ca_{21}Mn_4Sb_{18}$ structure type and play a large role in the good transport properties of this compound. The valence band states near the Fermi level are largely composed from atoms in this motif. The stability of this structure is confirmed by DFT calculations, which also show that the structure is sustained by the magnetic ordering of the *d*-electrons of Mn. A geometry optimization imposing no magnetization leads to the dimerization of Mn atoms and to a substantial distortion of the crystal.

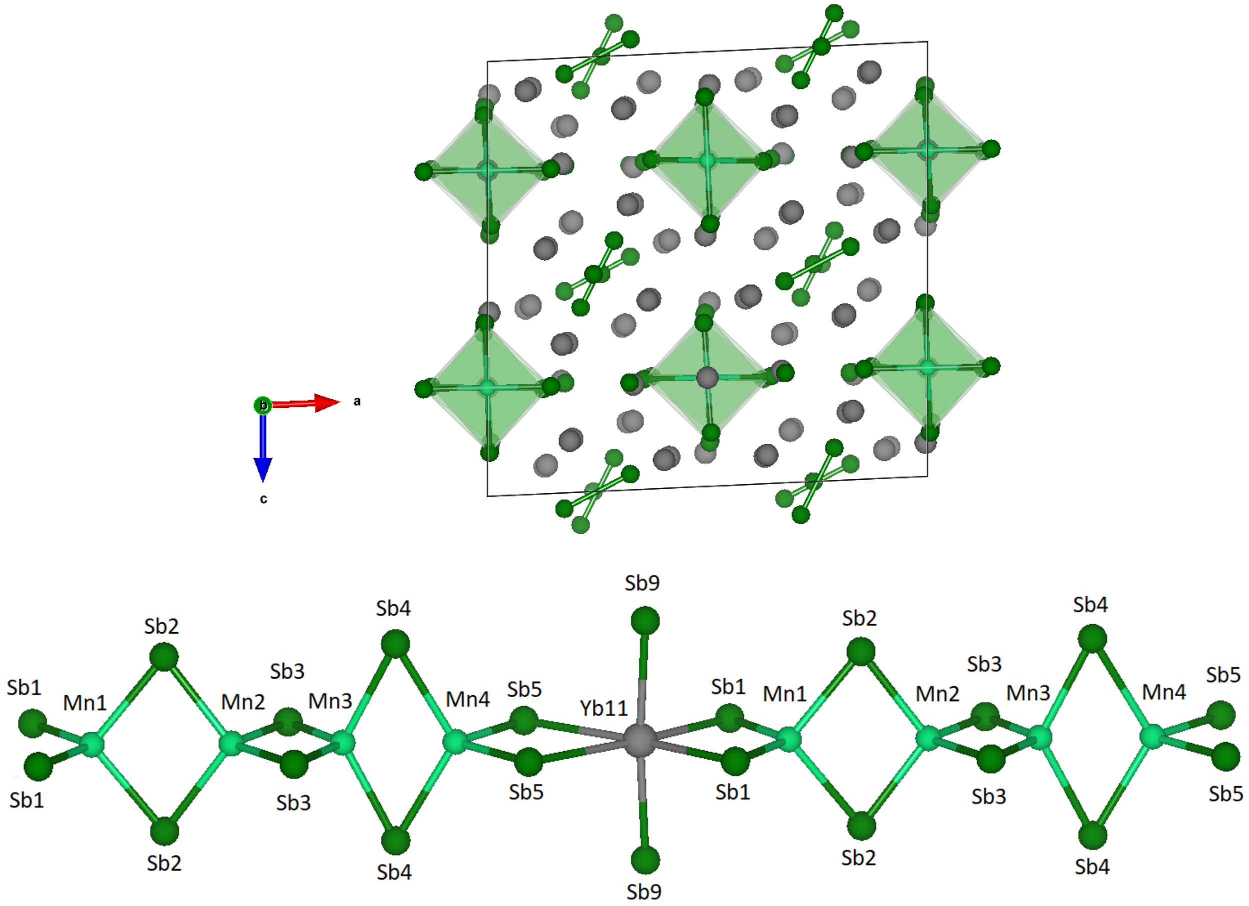

Figure 2: A view of the $Yb_{21}Mn_4Sb_{18}$ structure highlighting the $[Mn_4Sb_{10}]^{22-}$ units and $[Sb_2]^{4-}$ dimers projected down the *b*-axis, shown without disorder for clarity. A view of the overarching 21-4-18 motif of $[Mn_4Sb_{10}]^{22-}$ tetramer units linked through an octahedrally coordinated Yb atom.

The final structural solution determined experimentally indicated positional disorder and deficiencies on several sites and the intrinsic nature of these disorder and deficiencies was verified with several independent high quality crystals. Initially, a perfectly ordered model of the crystal structure was assumed, however, residual electron density was found to gather close to the Yb11 site, between the Mn2/Mn3 sites, the Sb3 site, and the Sb9 site (shown in **Figure 2**). The magnitude of these residual densities was too large to ignore as noise (~6 - 8 $e^-/Å^3$) and due to their close proximity to existing sites (~1 Å), were modelled as site disorder (Yb12, Mn5, Sb11, Sb10). **Table S2** (**SI**) provides the atomic positions and atomic displacement parameters for all of the sites. Starting with the Yb site disorder, analysis of all Yb – Sb polyhedral volumes show that the Yb11 site has the largest polyhedral volume out of all of the Yb sites which allows for rattling of the Yb atom between the extremum positions of the Yb11 site and Yb12 site. The occupancies of these two sites were allowed to refine freely and converged to be 91.6(2)% and 2.5(1)% respectively, making the overall Yb site slightly deficient. When the Yb11 or Yb12 sites are not occupied, the Sb9 atoms are able to relax closer to the center of the octahedron to the Sb10 position, causing the Sb site to be disordered as well. The Sb site is disordered only when there is a Yb deficiency, and therefore, the Sb9/Sb10 site were refined to be occupied (91.6(2)% + 2.5(1)% = 94.2(2)%) 94.2(2)%/5.8(2)% respectively. The **SI** displays a close-up of the Yb11/Yb12 and Sb9/Sb10 disorder (**Figure S3**) and the second region of disorder (**Figure S4**), which occurs in the middle of the tetramer chain. Residual electron density was observed to gather near the middle of the Mn2/Mn3 atoms and the Sb3 site from the refinement. In the case that the Mn5 site is occupied, it is not possible for any of the Mn2 and Mn3 sites to be occupied, for the resultant bond distance would be too small (Mn3 – Mn5: 1.138(2) Å, Mn2 – Mn5: 1.587(2) Å). During the refinement, the Mn2/Mn3 atoms were assumed to contribute equally to the Mn5 site and were constrained to have the same site occupancy. Therefore, the refined occupancy of the Mn2/Mn3/Mn5 sites are 92.3(3)%/92.3(3)%/7.7(3)% respectively. Upon occupation of the Mn5 site, the rigidity of the tetramer chain falls apart because of the disconnect (see **SI**) and the Sb3 atoms are able to relax further out to occupy the Sb11 position. The Sb11 position was restrained to have the same occupancy as the Mn5 atom resulting in the Sb3/Sb11 position being occupied 92.3(3)%/7.7(3)% respectively.

Elemental Composition

Ball-milling of the elemental reagents followed by spark plasma sintering resulted in >95% dense pellets. Secondary electron imaging confirms the high density of the sample and elemental mapping reveals a homogeneous distribution of elements after processing (**Figure 3**). Compositions of the pelletized samples were found to be within ~1 at. % of nominal stoichiometry (see **SI**, **Table S3**) according to EDS and WDS studies for all samples.

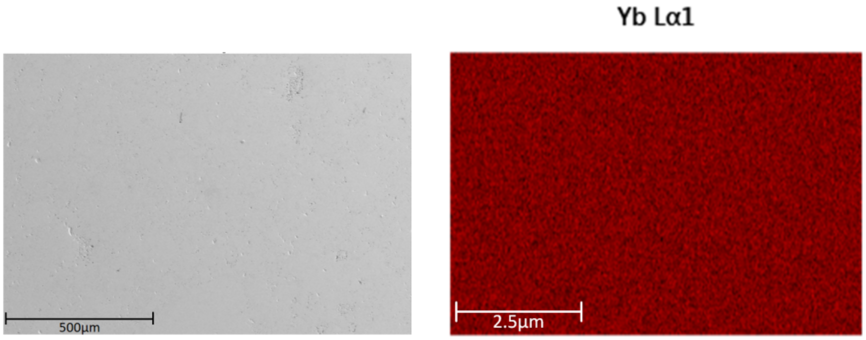

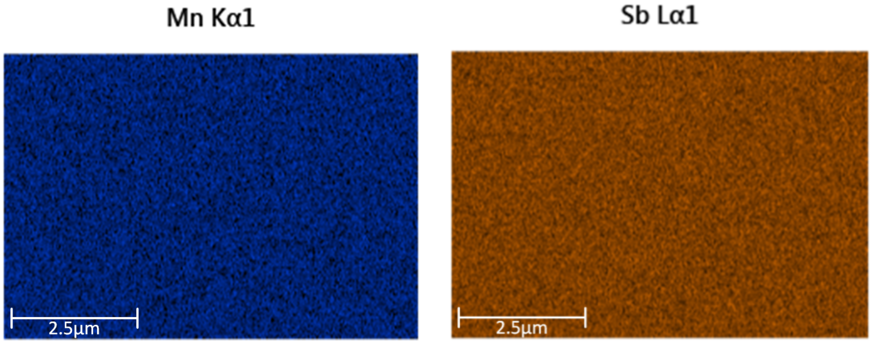

Figure 3: Secondary electron image collected with 20 kV electron beam confirming the high density of the polycrystalline samples. Elemental mapping of Yb (red), Mn (blue), and Sb (orange) shows homogeneity across the whole sample.

Rietveld refinement (see **SI, Table S4**) of the synchrotron powder X-ray diffraction data indicate that the powder samples are single phase (**Figure 4a**). The lattice parameters obtained from Rietveld refinement (*a* = 17.02725(9), *b* = 17.04802(9), *c* = 16.77150(9) Å, β = 92.7936(4)˚, 298 K) were observed to be larger than those obtained in the single crystal refinement (*a* = 16.930(3), *b* = 17.029(3), *c* = 16.693(3) Å, β = 92.61(3)˚, 100 K) and attributed to the difference in data collection temperature. The positional disorder on the Yb11/12, Sb9/10, Mn2/3/5, and Sb3/Sb11 sites proved difficult to refine from powder X-ray diffraction and gave inconsistent results, likely due to the large overlap of peaks in the powder pattern leading to large displacement factors. These sites could not be reliably determined to exist from powder diffraction and were therefore removed from the Rietveld refinement. The Yb11 site did not show any appreciable deficiency and was assumed to be fully occupied. The Mn2 and Mn3 sites refined best being deficient and were constrained to have equal occupancies which refined to be 94(1)%.

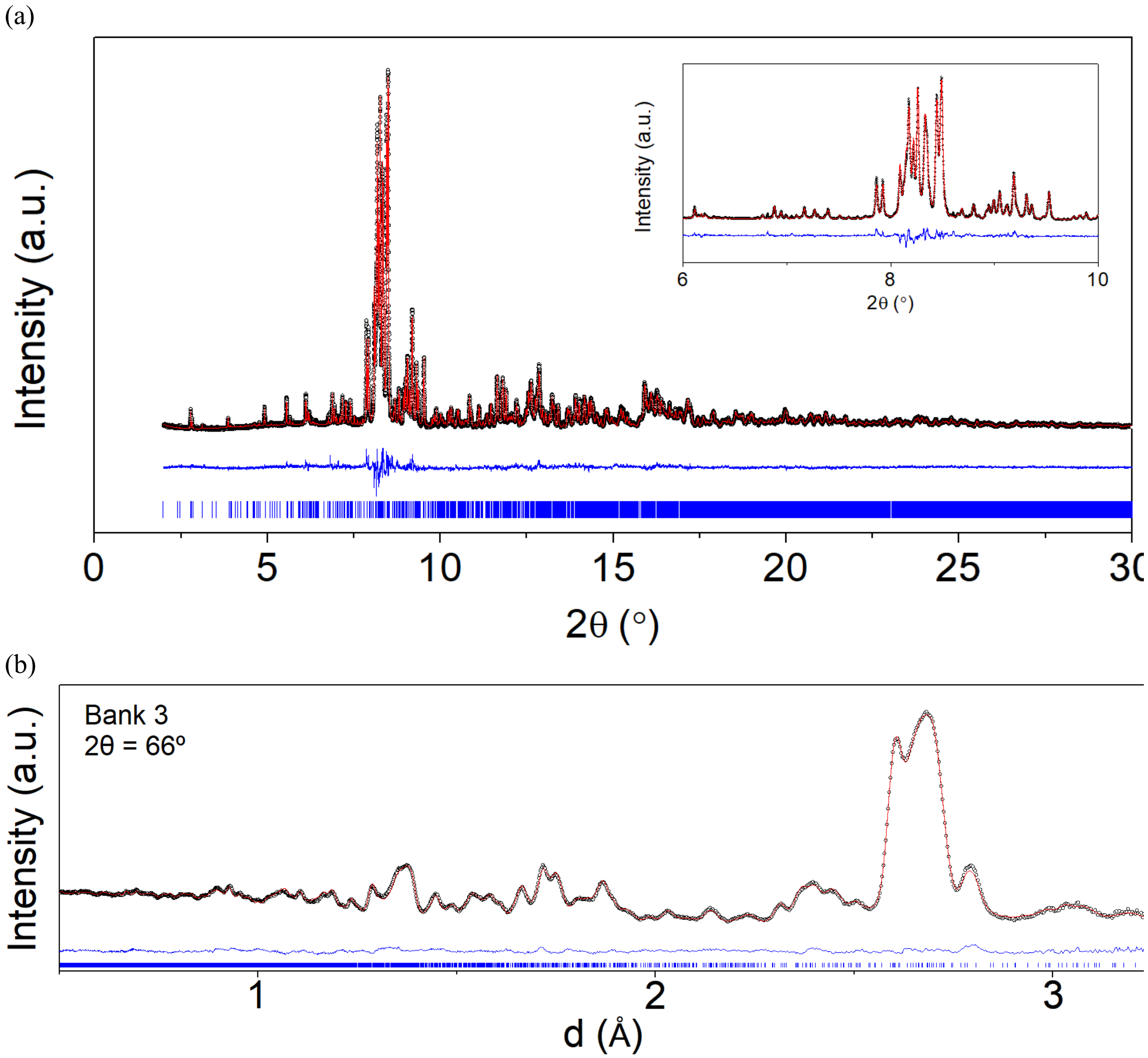

Figure 4: (a) Rietveld refinement of synchrotron X-ray diffraction (λ = 0.412736 Å) data at room temperature for $Yb_{21}Mn_4Sb_{18}$ and (b) time-of-flight neutron diffraction. Refined model is shown in red, experimental data as black dots, and the difference curve is shown in blue. The expected peak positions are shown by the blue tick marks.

The structural disorder was further characterized through total neutron scattering studies. Time-of-flight neutron diffraction data (**Figure 4b**) were collected using a high Q range for pair distribution function analysis, refer to **SI**, **Figure S5** for the S(Q) - 1 function. The converted G(r) function shows distinct features out to large distances (>150 Å) indicating a high degree of crystallinity in the sample.

The total intensity of a peak in G(r) is given by the expression: $I_{tot} = \sum_{xy} N_{xy} b_x b_y$ where N_{xy} is the number of atom pairs that contribute to the peak and b_x, b_y are the scattering lengths of atom x, atom y. The broadness of each peak in the PDF is a result of the contribution of many different atomic pairs, where the distribution of atom pairs is exemplified in the short-r region shown in **Figure 5** (selected bond distance ranges obtained from crystallography studies presented in **Table 1**).

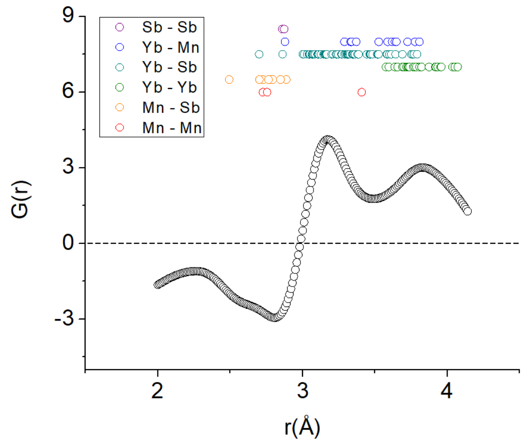

Figure 5: Short-r region (2 Å - 4 Å) of G(r) for $Yb_{21}Mn_4Sb_{18}$ at 298 K. Peaks below 2 Å were considered to be unphysical and were not included in the analysis. Distances obtained from X-ray crystallography are plotted on here for reference.

Table 1: Distance Ranges for Selected Nearest Neighbour Atom Pairs Determined from Single Crystal X-ray Studies of $Yb_{21}Mn_4Sb_{18}$.

Atom Pair	**Distance Range**
Mn – Sb	2.496(1) Å – 2.888(1) Å
Mn – Mn	2.721(3) Å – 3.409(3) Å
Sb – Sb	2.860(1) Å – 2.872(1) Å
Yb – Sb	2.68(1) Å – 3.791(1) Å
Yb – Mn	2.89(3) Å – 3.807(1) Å
Yb – Yb	3.576(1) Å – 4.071(1) Å

From the 2.50 Å to 3.00 Å region, the PDF is seen to be largely made up of Mn – (Mn,Sb) pairs. The negative scattering length of Mn is apparent from the negative peak around 2.80 Å. As we progress to the higher r atom pairs, the large positive scattering lengths of Yb and Sb along with the high number of Yb – Sb atom pairs results in the upswing and peak at 3.17 Å. As the onset of the Yb – Mn pairs come into play and the number of Yb – Sb atom pairs drop, the intensity starts to decrease causing the downturn found at 3.48 Å. Finally, the appearance of the Yb – Yb pairs results in the peak at 3.83 Å.

In total, the G(r) data were fit using three different models as seen in **Figure 6**. The first two models assumed the fully ordered crystal structure with isotropic atomic displacement factors (ADFs) and anisotropic ADFs (**Figure 6a**, **Figure 6b** respectively). The last model employed the disordered crystal structure, obtained from X-ray diffraction, using anisotropic ADFs (**Figure 6c**). The range of fitting for the G(r) function was set at a constant 20 Å.

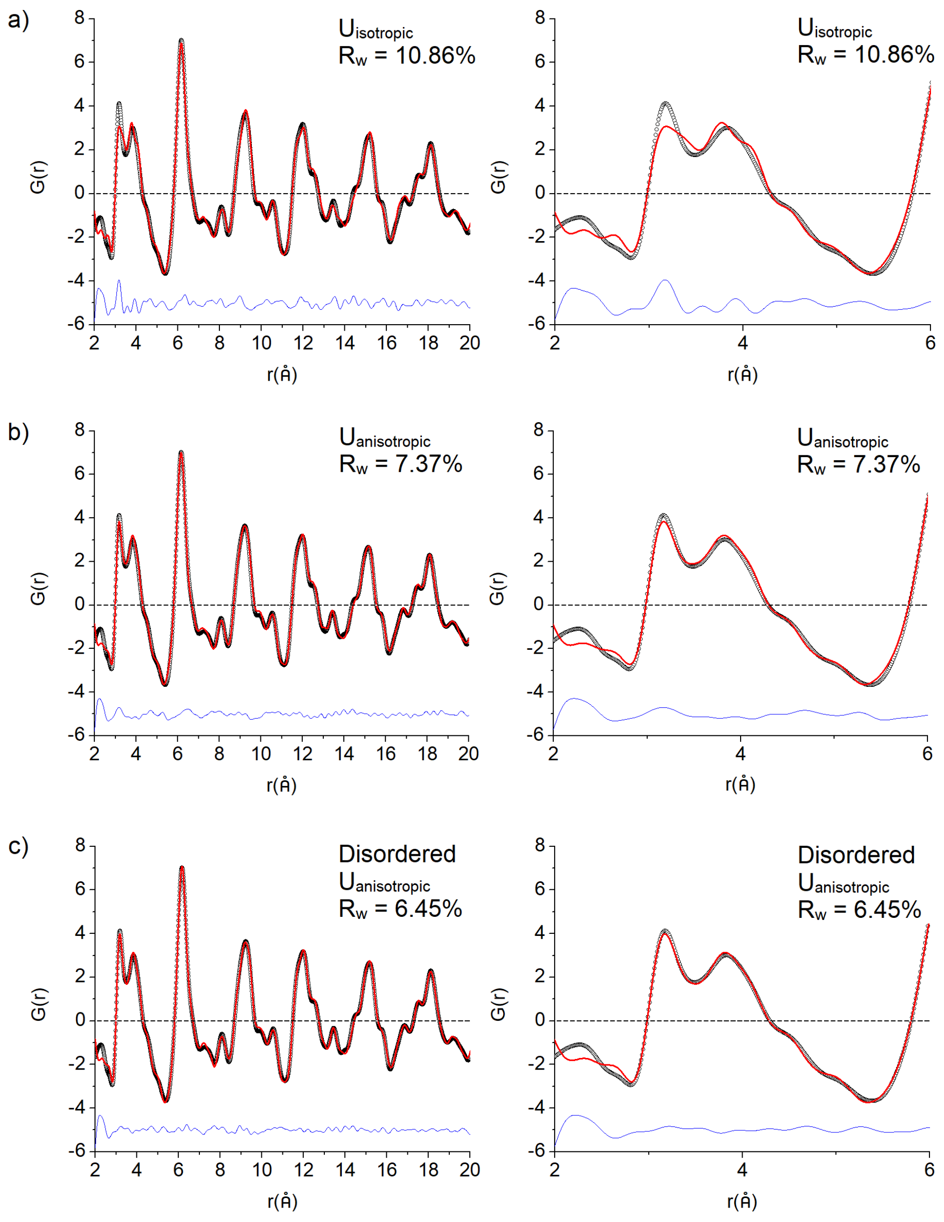

Figure 6: Pair distribution function (G(r)) refinement using three different models for $Yb_{21}Mn_4Sb_{18}$: (a) ordered structure isotropic ADFs, (b) ordered structure anisotropic ADFs, and (c) disordered crystal structure using anisotropic ADFs. Data were collected at 298K.

The isotropic model fit was poor with an $R_w = 10.86\%$. Most notably, the peak around 3.15 Å, made up from Yb – Sb pairs, is severely underestimated. The data were thus fit with anisotropic ADFs for all atoms. Significant improvements to the fit were obtained with $R_w = 7.37\%$ and gave much better descriptions of the Yb – Sb, Yb – Yb, and Yb – Mn pairs. To determine the contribution of disorder to the structure, the last structural model employed the Yb11/Yb12 and Sb9/Sb10 rattling, the Mn2/Mn3/Mn5 disorder, and Sb3/Sb11 disorder along with anisotropic ADFs. The drop in R_w value to 6.45% can be attributed to the disorder in the structure, supporting the results of the X-ray diffraction experiments. The improved fit can be observed in the short-r region of G(r) where the intensity description is seen to provide a better fit the experimental data.

Electronic Structure Calculations

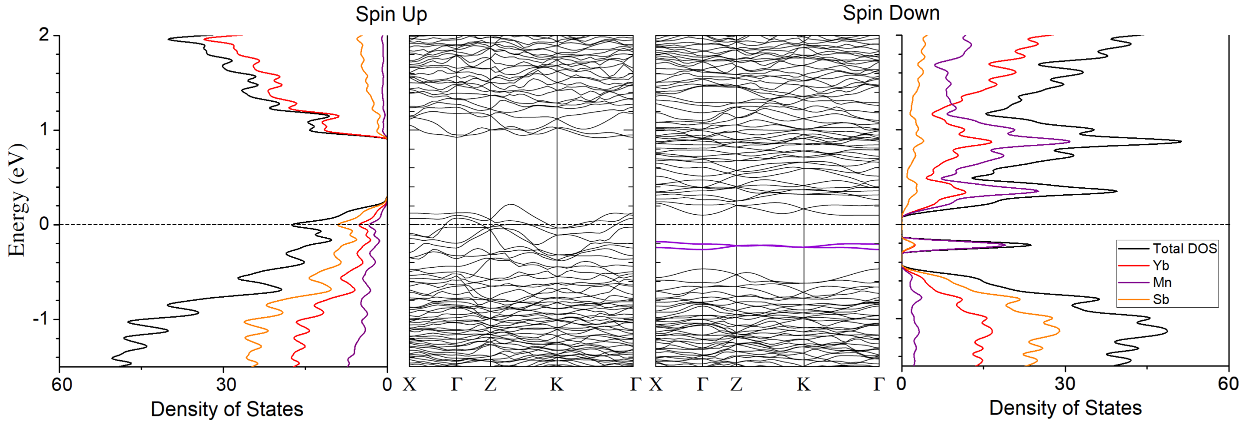

Figure 7: Spin-polarized band structure and density of state calculations for $Yb_{21}Mn_4Sb_{18}$. Fermi level is located at E = 0.

Spin-polarized electronic structure calculations (**Figure 7**) show that the Fermi level lies in the top part of the spin-up valence band (see **SI**, **Figure S6** for a close-up view of the spin up states near the Fermi level), making the ideal system a highly doped p-type semiconductor. The conducting hole states are delocalized over all the three atomic species, with a prevalent Sb character. For the spin-down polarization, the Fermi level is found in the gap between two occupied bands strongly localized on Mn and a low-lying conduction band with the participation of Mn and Yb states. Because of the close proximity of the Mn states to the Fermi level, doping studies of the transition metal should be pursued to push these states closer to the Fermi level to increase the Seebeck coefficient. Alternatively, the Fermi level can be shifted by doping, to align with these isolated Mn states. Conversely raising the Fermi level to higher energy would place it in the spin-down conduction band, thus changing the character of transport from p-type to n-type. Overall, these calculations show that at low temperature, $Yb_{21}Mn_4Sb_{18}$ acts as a p-type degenerate semiconducting material that can sustain spin-polarized current. In general, this is a disadvantage for the thermoelectric efficiency, as only half the electrons contribute to transport: engineering the band structure to add electrons with opposite spin to contribute to transport may substantially enhance zT.

Furthermore, we studied the effect of Na doping by considering 21 replicas of the $Yb_{21-x}Na_xMn_4Sb_{18}$ system with x = 0.5, in which Na substitutes Yb in each symmetrically inequivalent position. This Na concentration is about twice as much as that probed in experiments. Total energy differences among the various systems are smaller than 0.17 eV, thus indicating that Na may substitute any site during high temperature synthesis. The presence of Na reduces the cell magnetization from 36 to 35 μ_B/cell and produces a rigid shift of the spin-up density of states of about 0.1 eV, leaving the spin-down states nearly unperturbed (see **SI**, **Figure S7**).

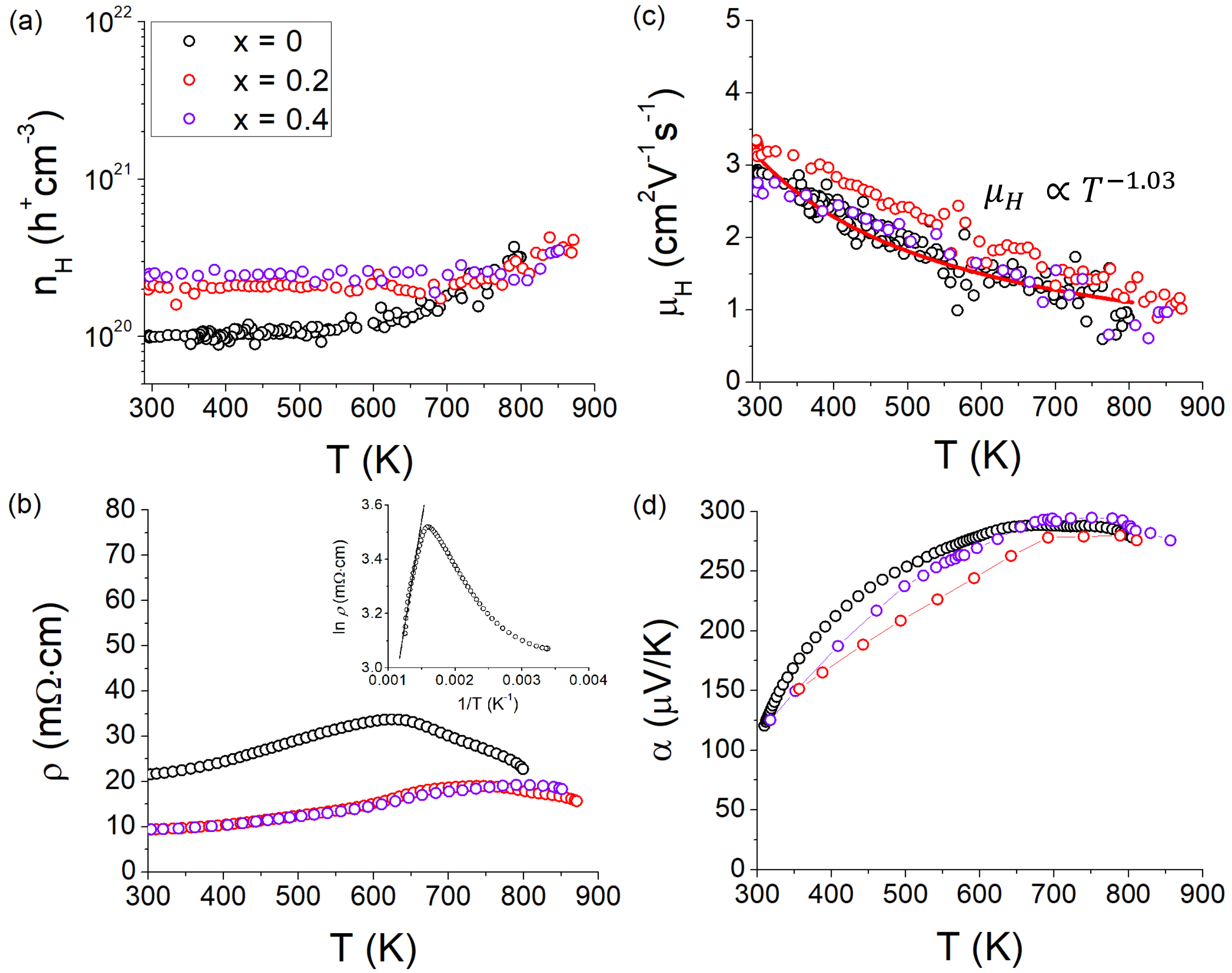

Figure 8: Thermoelectric transport properties of $Yb_{21-x}Na_xMn_4Sb_{18}$. (a) Temperature dependence of carrier concentration, (b) resistivity (inset shows slope of band gap determination), (c) Hall mobility (μ_H) (red line shows power law fit of $\mu_H \propto T^{-1.03}$ which is close to expected 1/T dependence of mobility for degenerate semiconductors[33]), and (d) Seebeck coefficient.

Temperature dependent Hall measurements reveal (**Figure 8a**) a large carrier concentration on the order of 10^{20} cm^{-3} confirming the degenerate semiconducting nature of 21-4-18. With increasing Na content, there is a corresponding increase in carrier concentration, however it is likely that the Na amount (x = 0.4) is slightly more than can be accommodated by the structure as there is not a complete correspondence between the x = 0.2 and x = 0.4 samples. No traces of impurities could be detected in powder X-ray diffraction or SEM for all samples. Attempts at increasing the Na doping further resulted in small impurities identified as $Yb_9Mn_{4.2}Sb_9$ and $Yb_{14}MnSb_{11}$ with Na also segregating at the grain boundaries. Once there is enough energy to thermally excite electron-hole pairs, the carrier concentration can be seen to steadily increase with temperature for all samples. As the Fermi level probes deeper into the valence band with the increasing Na content, the amount of thermal energy necessary to excite carriers across the band gap increases, making the increase in carrier concentration occur at higher temperatures.

This phenomenon is carried over into the temperature dependence of resistivity (**Figure 8b**) where resistivity starts to bend over at the point of carrier concentration increase. The activation of electron-hole pairs increases carrier concentration and lowers the resistivity. The temperature dependence of the resistivity in the region after activation will largely be dominated by the exponential dependence of the carrier concentration[32] and should follow the relationship (**Equation 3**):

$$\rho = Ae^{E_g/2k_BT} \tag{3}$$

where A is a constant, E_g is the band gap, k_B is Boltzmann's constant. From this model, a band gap of ~0.4 eV is calculated for the undoped sample.

Generally, the mobility (**Figure 8c**) is relatively unaffected by the Na doping and remains roughly constant over all samples. The decrease with increasing temperature is indicative of an increase in scattering interactions such as electron-phonon interactions. The temperature dependence of mobility should be given by a power law. Assuming that only acoustic phonon scattering limits the relaxation time, the mobility is expected to decrease as T^{-x} where $1 \leq x \leq 1.5$ where the limit of x = 1 is seen for highly degenerate samples (close to the observed $T^{-1.03}$) and x = 1.5 is obtained for a nondegenerate electron gas.[33]

Lastly, the temperature dependence of the Seebeck coefficient is given in **Figure 8d** and seems to be relatively unaffected by the increase in carrier concentration due to a corresponding increase in effective mass (see below). The presence of the maximum in the Seebeck data as a function of T agrees well with the carrier concentration data. Bipolar conduction will result in a drop of Seebeck coefficient leading to the maximum observed in all samples. Goldsmid and Sharp were able to formulate an analytical expression ($E_g = 2e|\alpha|_{max}T_{max} = 0.394$ eV) relating the band gap (E_g), maximum Seebeck coefficient ($|\alpha|_{max}$), and the temperature of the peak (T_{max}).[34] The band gap value determined from the DFT calculations is around 0.3 eV, which is in good agreement with the experimental band gap values determined from resistivity and Seebeck coefficient.

From the electronic structure calculations, the Fermi level is seen to reside in an area where electrical transport is mediated by multiple bands. Some of these bands are flat, thus providing substantial contribution to the Seebeck coefficient, while a band with higher curvature at the Γ point sustains mobility (**Figure S6**). Although the single parabolic band (SPB) model[35] would not capture the full complexity of the full electronic structure, it is a common, powerful tool for characterizing thermoelectric transport, which can provide insight into the possible ways to enhance thermoelectric efficiency such as carrier concentration optimization. The model was applied at 600K so that minority carrier concentration remains negligible and acoustic phonon scattering limits the carrier mobility ($\lambda = 0$). The relationship between carrier concentration and the Seebeck coefficient was used to calculate the effective mass using the Pisarenko plot shown in **SI**, **Figure S8**. According to SPB model, the x = 0.4 sample has a higher effective mass ($m^* = 5.70\ m_e$) than the other two samples ($m^* = 3.73\ m_e$) which may be due to the Fermi level being situated in a local area of flat curvature.

The Seebeck coefficient (**Equation 4**) and carrier concentration (**Equation 5**) were calculated through evaluation of the Fermi-Dirac integral $F_j(\eta)$ (**Equation 6**).

$$\alpha = \frac{k}{e}\left(\frac{2F_1(\eta)}{F_0(\eta)} - \eta\right) \tag{4}$$

$$n = 4\pi \left(\frac{2m^* k_b T}{h^2}\right)^{3/2} F_{1/2}(\eta) \tag{5}$$

$$F_j(\eta) = \int_0^\infty \frac{\zeta^j d\zeta}{1 + \exp(\zeta - \eta)} \tag{6}$$

where η is the reduced chemical potential, ζ is the reduced carrier energy and j is the order of the Fermi-Dirac integral. The Hall carrier concentration (n_H) can be related to the carrier concentration (n) by **Equation 7**:

$$n_H = \frac{n}{r_H} \tag{7}$$

where r_H is the Hall factor (**Equation 8**), calculated from:

$$r_H = \frac{3}{2} F_{1/2}(\eta) \frac{F_{-1/2}(\eta)}{2F_0^2(\eta)} \tag{8}$$

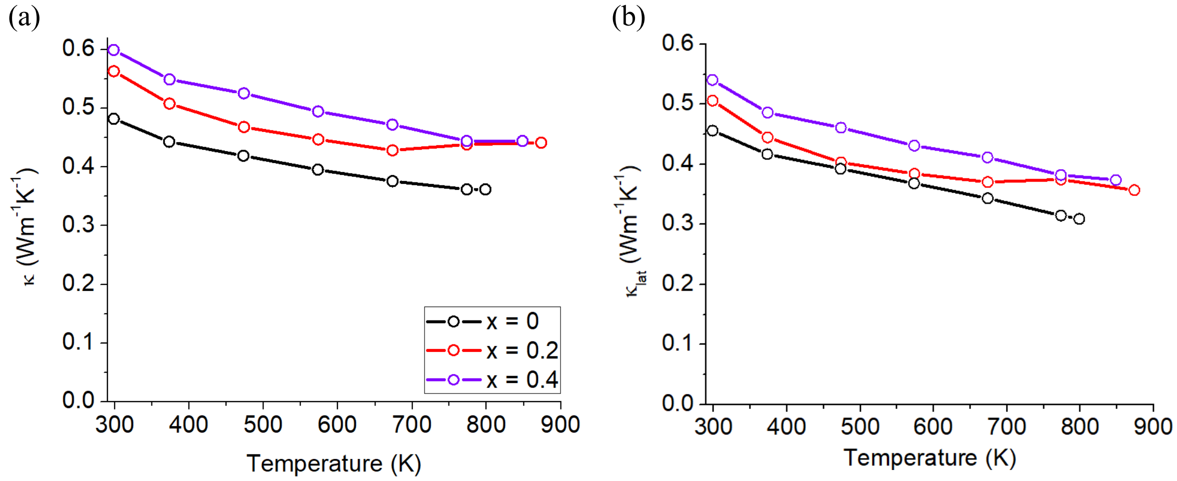

Figure 9: (a) Total thermal conductivity and (b) lattice thermal conductivity of $Yb_{21-x}Na_xMn_4Sb_{18}$ (x = 0, 0.2, 0.4).

Thermal conductivity (κ) data (**Figure 9**) were calculated from obtained measurements of thermal diffusivity (**Equation 9**):

$$\kappa = D\rho C_p \tag{9}$$

where D is the thermal diffusivity, ρ is the density of the sample, and C_p is the heat capacity. The Dulong-Petit law was used to estimate the heat capacity ($C_p = 0.177\ Jg^{-1}K^{-1}$ for the undoped sample). The total thermal conductivity (**Figure 9a**) is primarily made up of two components: the electronic contribution (κ_e) and the lattice (κ_l). According to the Wiedemann-Franz relationship, $\kappa_e = L\sigma T$, the electronic component can be subtracted from the total thermal conductivity to yield the lattice thermal conductivity (**Figure 9b**). The small increase in thermal conductivity with respect to increasing Na doping is attributed to Na atoms filling in the Yb vacancies. By filling in the vacancies (which would act as phonon scattering centers) the thermal conductivity of the system should slightly increase. In general, the low values in thermal conductivity are the result of the phonon mean free path being limited by the number of atoms in the unit cell and the large degree of structural disorder within the material.

Figure of Merit

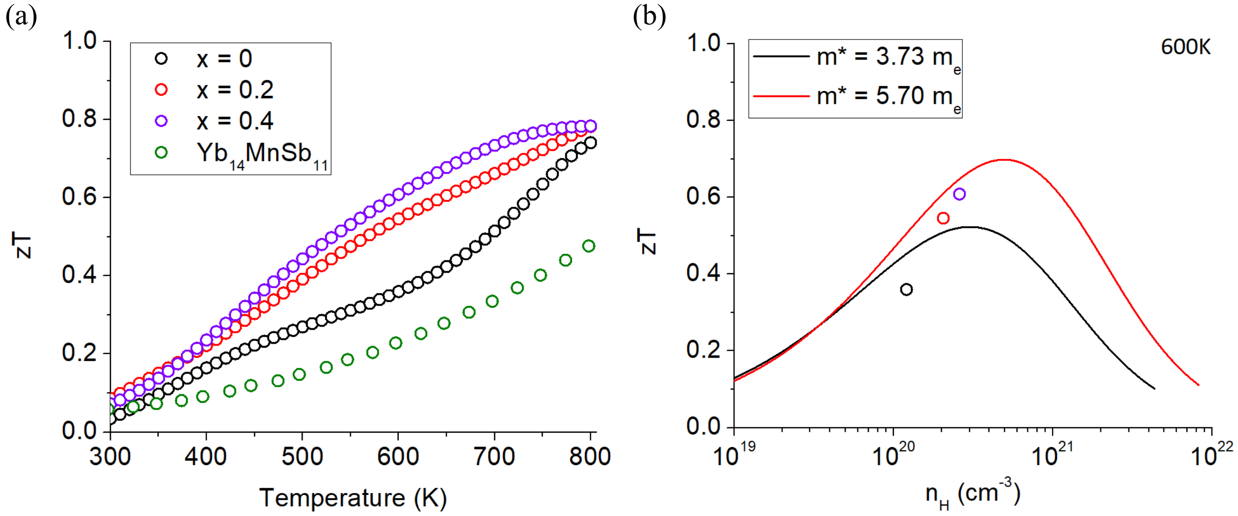

Figure 10: (a) Temperature dependent thermoelectric figure of merit, zT for $Yb_{21-x}Na_xMn_4Sb_{18}$ (x = 0, 0.2, 0.4). A maximum value of 0.74 was obtained at 800 K. (b) Single parabolic band model fit (right) at 600 K using $m^* = 3.73$ m_e, $\mu_0 = 2.31$ $cm^2V^{-1}s^{-1}$, and $\kappa_l = 0.38$ $Wm^{-1}K^{-1}$ in black and $m^* = 5.70$ m_e, $\mu_0 = 1.97$ $cm^2V^{-1}s^{-1}$, and $\kappa_l = 0.43$ $Wm^{-1}K^{-1}$ in red.

The thermoelectric figure of merit zT was calculated using polynomial fits to α, ρ, κ. As seen in **Figure 10a**, a maximum zT $\approx$ 0.8 was obtained at 800 K. The obtained zT was fit to the single parabolic band model (**Figure 10b**). The theoretical zT was calculated from **Equations 10 – 13**:

$$\mathrm{zT} = \frac{\alpha^2}{L + \frac{1}{\psi\beta}} \tag{10}$$

$$L = \frac{k^2}{e^2}\frac{3F_0(\eta)F_2(\eta) - 4F_1^2(\eta)}{F_0^2(\eta)} \tag{11}$$

$$\beta = \frac{\mu_0\left(\frac{m^*}{m_e}\right)^{\frac{3}{2}}T^{\frac{5}{2}}}{\kappa_L} \tag{12}$$

$$\psi = \frac{8\pi e}{3}\left(\frac{2m_e k}{h^2}\right)^{\frac{3}{2}} F_0(\eta) \tag{13}$$

The values used for effective mass (m^*), intrinsic mobility (μ_0), and lattice thermal conductivity (κ_L) were all obtained from the experimental data at 600 K for the SPB model. As seen from the model, the carrier concentrations obtained are close to the optimal carrier concentration predicted to give the largest zT.

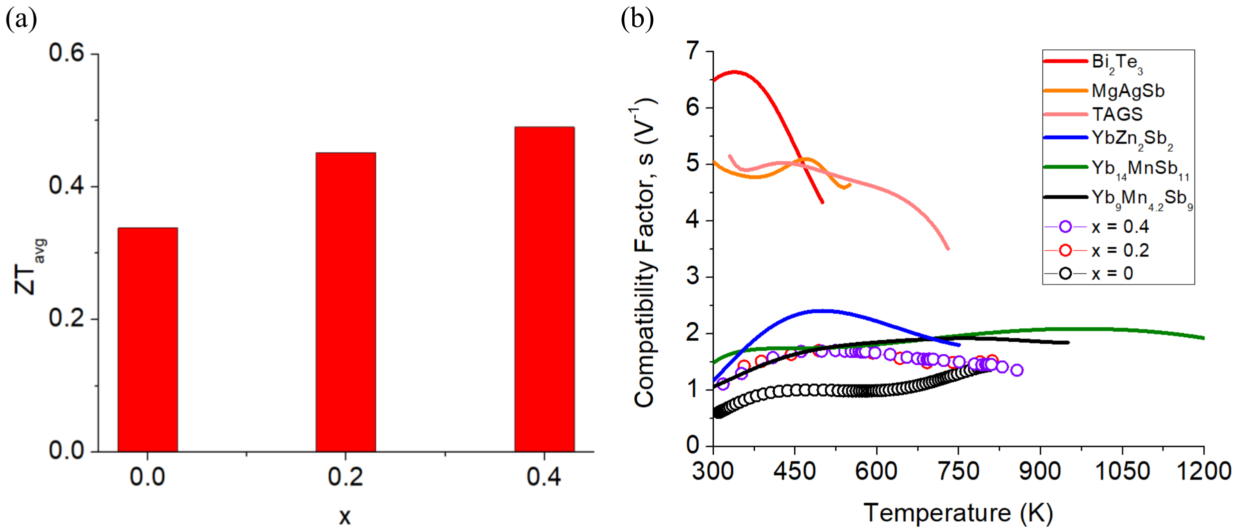

Figure 11: Practical considerations of $Yb_{21-x}Na_xMn_4Sb_{18}$ in device segmentation showing (a) an increase of ZT_{avg} with Na doping while (b) being compatible with other high zT materials. Compatibility factor was calculated from Seebeck coefficients and zT, taken from: Yu et al. (Bi_2Te_3),[36] Zhao et al. (MgAgSb),[37] Schröder et al. (TAGS),[38] Zevalkink et al. ($YbZn_2Sb_2$),[39] Brown et al. ($Yb_{14}MnSb_{11}$),[7] Bux et al. ($Yb_9Mn_{4.2}Sb_9$).[29]

For practical applications, a high peak zT within a narrow temperature range is often not enough to realize a high efficiency. Instead, efficiency of the thermoelectric module requires a large average zT as well as similar compatibility factors (s) of the segmented materials. With increasing amounts of Na doping, $Yb_{21-x}Na_xMn_4Sb_{18}$ experiences an increase in zT across the whole temperature range, yielding a larger ZT_{avg} calculated from the integration method (**Figure 11a**, $ZT_{avg} = 0.34$ for x = 0, $ZT_{avg} = 0.49$ for x = 0.4). For optimum device efficiency, the compatibility factors of the segmented materials should be within a factor of 2.[40] Here, ZT_{avg} refers to the performance of a device whereas lower case zT indicates the material performance. The compatibility factor (**Figure 11b**) of the Na-doped samples is much greater at low temperatures compared to the intrinsic sample but ends up with similar compatibility factor at high temperature to that of $Yb_{14}MnSb_{11}$ due to the similarity of zT and Seebeck. With the Na doping, this material has become much more compatible with other p-type thermoelectric materials at the lower temperatures, making it more viable for segmentation and potentially increasing the efficiency due to a better electrical and thermal impedance matching.

Summary

The complex Zintl phase, $Yb_{21}Mn_4Sb_{18}$, has been successfully synthesized through high temperature annealing followed by spark plasma sintering, resulting in phase pure powder according to synchrotron powder diffraction. Methods for single crystal growth have also been elucidated and single crystal X-ray diffraction studies reveal the disordered nature of this phase on multiple Yb, Mn, and Sb sites and within the $[Mn_4Sb_{10}]^{22-}$ tetramer units. The structural disorder was supported with total neutron scattering experiments using pair distribution function analysis which complement and agree with the X-ray scattering experiments. The structure consists of a $[Mn_4Sb_{10}]^{22-}$ unit, 2 $[Sb_2]^{4-}$ dimers, 4 isolated Sb^{3-} anions, and 21 Yb^{2+}, and can be described within the Zintl-Klemm electron counting scheme as a Zintl phase. Transport property measurements and DFT calculations show that $Yb_{21}Mn_4Sb_{18}$ behaves as a heavily doped p-type semiconductor with large carrier concentration (~10^{20} cm^{-3}), high Seebeck coefficient (~290 µV/K) and low thermal conductivity (~0.4 $Wm^{-1}K^{-1}$). The transport properties were modelled with a single parabolic band model assuming acoustic phonon scattering and the carrier concentration was optimized according to the composition, $Yb_{21-x}Na_xMn_4Sb_{18}$ (x = 0, 0.2, 0.4). The large effective mass (5.70 m_e) obtained by probing the Fermi level deeper through Na doping into the hole conduction band have shown an overall increase in zT across the whole temperature range for the x = 0.4 sample. Further optimization may be possible through doping or substitution of Yb, Mn, or Sb in this structure type to change the band structure in a favourable way. A maximum zT $\approx$ 0.8 at 800K is obtained for the x = 0.4 sample and ZT_{avg} increases from 0.34 to 0.49 compared to the intrinsic sample.

Acknowledgements

The authors acknowledge Modern Methods in Rietveld Refinement for Structural Analysis (MMRRSA) 2018 for beamline time at ORNL-SNS and ANL and Katherine Page, Jue Liu, Joerg Neuefeind at NOMAD for useful discussion. We thank Christopher J. Perez for his help in measuring transport properties, Elizabeth L. Kunz Wille and Dr. Jim Fettinger for useful crystallography discussions and NSF DMR-1709382 for funding. Some of this work was performed at the California Institute of Technology/Jet Propulsion Laboratory under contract with the National Aeronautics and Space Administration. JPL affiliates were supported by the NASA Science Missions Directorate's Radioisotope Power Systems program. Calculations were performed on Comet at the San Diego Supercomputer Center, using the Extreme Science and Engineering Discovery Environment (XSEDE), which is supported by National Science Foundation grant number ACI-1548562, allocation CHE190009.

Supporting Information

The Supporting Information is available free of charge on the ACS Publications website at DOI:

Experimental details and supporting figures: (CIF): $Yb_{21}Mn_4Sb_{18}$; (PDF): C2/c structure motif figures, Single crystal X-ray data collection and refinement parameters, Atomic coordinates and displacement parameters determined from single crystal and synchrotron X-ray diffraction, Picture of single crystal, Close-up view of disordered sites, Compositional analysis on pressed pellets (WDS & EDS), Rietveld refinement results, Structure Function (S(Q)-1) for PDF, Close-up view of the spin-up band structure near E_f, DFT Calculations on Na-doped $Yb_{21}Mn_4Sb_{18}$, Pisarenko Plot for SPB model.

Corresponding Author

*E-mail: smkauzlarich@ucdavis.edu

Notes

The authors declare no competing financial interest.

References

[1] Toberer, E. S.; May, A. F.; Snyder, G. J. Zintl Chemistry for Designing High Efficiency Thermoelectric Materials. *Chemistry of Materials*. **2010**, *22*, 624 - 634.

[2] Ovchinnikov, A.; Bobev, S. Zintl phases with group 15 elements and the transition metals: A brief overview of pnictides with diverse and complex structures. *Journal of Solid State Chemistry*. **2019**, *270*, 346 - 359.

[3] Kauzlarich, S. M.; Brown, S. R.; Snyder, G. J. Zintl phases for thermoelectric devices. *Dalton Transactions*. **2007**, *21*, 2099 - 2107.

[4] Kauzlarich, S. M. Chemistry, Structure, and Bonding of Zintl Phases and Ions. Wiley-VCH: New York, 1996.

[5] Rauscher, J. F.; Cox, C. A.; Yi, T.; Beavers, C. M.; Klavins, P.; Toberer, E. S.; Snyder, G. J.; Kauzlarich, S. M. Synthesis, structure, magnetism, and high temperature thermoelectric properties of Ge doped $Yb_{14}MnSb_{11}$. *Dalton Transactions*. **2010**, *39*, 1055 - 1062.

[6] Möchel, A.; Sergueev, I.; Wille, H.-C.; Juranyi, F.; Schober, H.; Schweika, W.; Brown, S. R.; Kauzlarich, S. M.; Hermann, R. P. Lattice dynamics in the thermoelectric Zintl compound $Yb_{14}MnSb_{11}$. *Physical Review B*. **2011**, *84*, 184303-1 - 184303-10.

[7] Brown, S. R.; Kauzlarich, S. M.; Gascoin, F.; Snyder, G. J. $Yb_{14}MnSb_{11}$: New High Efficiency Thermoelectric Material for Power Generation. *Chemistry of Materials*, **2006**, *18*, 1873 - 1877.

[8] Toberer, E. S.; Cox, C. A.; Brown, S. R.; Ikeda, T.; May, A. F.; Kauzlarich, S. M.; Snyder, G. J. Traversing the Metal-Insulator Transition in a Zintl Phase: Rational Enhancement of Thermoelectric Efficiency in $Yb_{14}Mn_{1-x}Al_xSb_{11}$. *Advanced Functional Materials*, **2008**, *18*, 2795 - 2800.

[9] Snyder, G. J.; Christensen, M.; Nishibori, E.; Caillat, T.; Iversen, B. B. Disordered zinc in Zn_4Sb_3 with phonon-glass and electron-crystal thermoelectric properties. *Nature Materials*. **2004**, *3*, 458−463.

[10] Mozharivskyj, Y.; Janssen, Y.; Harringa, J. L.; Kracher, A.; Tsokol, A. O.; Miller, G. J. $Zn_{13}Sb_{10}$: A Structural and Landau Theoretical Analysis of Its Phase Transitions. *Chemistry of Materials*. **2006**, *18*, 822 - 831.

[11] Lo, C.-W. T.; Ortiz, B. R.; Toberer, E. S.; He, A.; Svitlyk, V.; Chernyshov, D.; Kolodiazhnyi, T.; Lidin, S.; Mozharivskyj, Y. Synthesis, Structure, and Thermoelectric Properties of α-Zn_3Sb_2 and Comparison to β-$Zn_{13}Sb_{10}$. *Chemistry of Materials*, **2017**, *29*, 5249 - 5258.

[12] Christensen, M.; Lock, N.; Overgaard, J.; Iversen, B. B. Crystal Structures of Thermoelectric n- and p-type $Ba_8Ga_{16}Ge_{30}$ Studied by Single Crystal, Multitemperature, Neutron Diffraction, Conventional X-

ray Diffraction and Resonant Synchrotron X-ray Diffraction. *Journal of American Chemical Society*. **2006**, *128*, 15657 - 15665.

[13] May, A. F.; Toberer, E. S.; Saramat, A.; Snyder, G. J. Characterization and analysis of thermoelectric transport in n-type $Ba_8Ga_{16-x}Ge_{30+x}$. *Physical Review B*. **2009**, *80*, 125205-1 - 125205-12.

[14] Chen, B.; Xu, J.-H.; Uher, C.; Morelli, D. T.; Meisner, G. P.; Fleurial, J.-P.; Caillat, T.; Borshchevsky, A. Low-temperature transport properties of the filled skutterudites $CeFe_{4-x}Co_xSb_{12}$. *Physical Review B*. **1997**, *55*, 1476 - 1480.

[15] Xia, S.-Q; Bobev, S. Zintl Phase Variations Through Cation Selection. Synthesis and Structure of $A_{21}Cd_4Pn_{18}$ (A = Eu, Sr, Ba; Pn = Sb, Bi). *Inorganic Chemistry*, **2008**, *47*, 1919 - 1921.

[16] Suen, N.-T.; Wang, Y.; Bobev, S. Synthesis, crystal structures, and physical properties of the new Zintl phases $A_{21}Zn_4Pn_{18}$ (A = Ca, Eu; Pn = As, Sb) – Versatile arrangements of [$ZnPn_4$] tetrahedra. *Journal of Solid State Chemistry*, **2015**, *227*, 204 - 211.

[17] Holm, A. P.; Olmstead, M. M.; Kauzlarich, S. M. The Crystal Structure and Magnetic Properties of a New Ferrimagnetic Semiconductor: $Ca_{21}Mn_4Sb_{18}$. *Inorganic Chemistry*. **2003**, *42*, 1973 - 1981.

[18] Xia, S.-Q.; Bobev, S. Diverse Polyanions Based on $MnBi_4$ and $MnSb_4$ Tetrahedra: Polymorphism, Structure, and Bonding in $Ca_{21}Mn_4Bi_{18}$ and $Ca_{21}Mn_4Sb_{18}$. *Inorganic Chemistry*, **2007**, *46*, 874 - 883.

[19] Canfield, P. C.; Kong, T.; Kaluarachchi, U. S.; Jo, N. H. Use of frit-disc crucibles for routine and exploratory solution growth of single crystalline samples. *Philosophical Magazine*, **2016**, *96*, 84 – 92.

[20] Sheldrick, G. M. SHELXL97 and SHELXS97, University of Gottigen, Germany, 1997.

[21] Neuefeind, J.; Feygenson, M.; Carruth, J.; Hoffmann, R.; Chipley, K. K. The Nanoscale Ordered Materials Diffractometer NOMAD at the Spallation Neutron Source SNS. *Nuclear Instruments and Methods in Physics Research B*. **2012**, *287*, 68 - 75.

[22] Farrow, C. L.; Juhas, P.; Liu, J. W.; Bryndin, D.; Božin, E. S.; Bloch, J.; Proffen, T.; Billinge, S. J. L. PDFfit2 and PDFgui: computer programs for studying nanostructure in crystals. *Journal of Physics Condensed Matter*. **2007**, *19*, 335219-1 - 335219-7.

[23] Wood, C.; Zoltan, D.; Stapfer, G. Measurement of Seebeck coefficient using a light pulse. *Review of Scientific Instruments*, **1985**, *56*, 719 - 722.

[24] Borup, K. A.; Toberer, E. S.; Zoltan, L. D.; Nakatsukasa, G.; Errico, M.; Fleurial, J.-P.; Iverson, B. B.; Snyder, G. J. Measurement of the electrical resistivity and Hall coefficient at high temperatures. *Review of Scientific Instruments*. **2012**, *83*, 123902-1 - 123902-7.

[25] Perdew, J. P.; Burke, K.; Ernzerhof, M. Generalized Gradient Approximation Made Simple. *Phys. Rev. Lett.* **1996**, *77*, 3865 – 3868.

[26] Monkhorst, H. J.; Pack, J. D. Special Points for Brillouin-Zone Integrations. **1976**, *13*, 5188 – 5192.

[27] Giannozzi, P.; Baroni, S.; Bonini, N.; Calandra, M.; Car, R.; Cavazzoni, C.; Ceresoli, D.; Chiarotti, G. L.; Cococcioni, M.; Dabo, I.; Dal Corso, A.; de Gironcoli, S.; Fabris, S.; Fratesi, G.; Gebauer, R.;

Gerstmann, U.; Gougoussis, C.; Kokalj, A.; Lazzeri, M.; Martin-Samos, L.; Marzari, N.; Mauri, F.; Mazzarello, R.; Paolini, S.; Pasquarello, A.; Paulatto, L.; Sbraccia, C.; Scandolo, S.; Sclauzero, G.; Seitsonen, A. P.; Smogunov, A.; Umari, P.; Wentzcovitch, R. M. QUANTUM ESPRESSO: a Modular and Open-Source Software Project for Quantum Simulations of Materials. *Journal of Physics: Condensed Matter*. **2009**, *21*, 395502-1 – 395502-19.

[28] Ruehl, R.; Jeitschko, W. New pnictides with Ce_2O_2S-type structure. *Materials Research Bulletin*, **1979**, *14*, 513 - 517.

[29] Bux, S. K.; Zevalkink, A.; Janka, O.; Uhl, D.; Kauzlarich, S.; Snyder, J. G.; Fleurial, J-. P. Glass-like lattice thermal conductivity and high thermoelectric efficiency in $Yb_9Mn_{4.2}Sb_9$. *Journal of Materials Chemistry A*, **2014**, *2*, 215 – 220.

[30] Xia, S.-Q.; Bobev, S. New Manganese-Bearing Antimonides and Bismuthides with Complex Structures. Synthesis, Structural Characterization, and Electronic Properties of $Yb_9Mn_{4+x}Pn_9$ (Pn= Sb or Bi). *Chemistry of Materials*, **2010**, *22*, 840 - 850.

[31] Ohno, S.; Zevalkink, A.; Takagiwa, Y.; Bux, S. K.; Snyder, G. J. Thermoelectric properties of the $Yb_9Mn_{4.2-x}Zn_xSb_9$ solid solutions. *Journal of Materials Chemistry A*, **2014**, *2*, 7478 - 7483.

[32] Kittel, C. Introduction to Solid State Physics, John Wiley & Sons, 1996.

[33] Ravich, U. I., Efimova, B. A., Smirnov, I. A. Semiconducting lead chalcogenides, Plenum Press, 1970.

[34] Goldsmid, H. J.; Sharp, J. W. Estimation of the Thermal Band Gap of a Semiconductor from Seebeck Measurements. *Journal of Electronic Materials*, **1999**, *28*, 869 - 872.

[35] Rowe, D. M. Materials, Preparation, and Characterization in Thermoelectrics, CRC Press, 2012.

[36] Yu, F.; Zhang, J.; Yu, D.; He, J.; Liu, Z.; Xu, B.; Tian, Y. Enhanced thermoelectric figure of merit in nanocrystalline Bi_2Te_3 bulk. *Journal of Applied Physics*, **2009**, *105*, 094303-1 - 094303-5.

[37] Zhao, H.; Sui, J.; Tang, Z.; Lan, Y.; Jie, Q.; Kraemer, D.; McEnaney, K.; Guloy, A.; Chen, G.; Ren, Z. High thermoelectric performance of MgAgSb-based materials. *Nano Energy*, **2014**, *7*, 97 - 103.

[38] Schröder, T.; Rosenthal, T.; Giesbrecht, N.; Nentwig, M.; Maier, S.; Wang, H.; Snyder, G. J.; Oeckler, O. Nanostructures in Te/Sb/Ge/Ag (TAGS) Thermoelectric Materials Induced by Phase Transitions Associated with Vacancy Ordering. *Inorganic Chemistry*, **2014**, *53*, 7722 – 7729.

[39] Zevalkink, A.; Zeier, W. G.; Cheng, E.; Snyder, J.; Fleurial, J. P.; Bux, S. Nonstoichiometry in the Zintl Phase $Yb_{1-\delta}Zn_2Sb_2$ as a Route to Thermoelectric Optimization. *Chemistry of Materials*, **2014**, *26*, 5710 – 5717.

[40] Snyder, G. J.; Ursell, T. S. Thermoelectric Efficiency and Compatibility. *Physical Review Letters*, **2003**, *91*, 148301-1 – 148301-4.

For Table of Contents